Stereoscopic PIV Study of a Simplified Landing Gear Model

Eric Salt, Marko Arežina, James Lepore, Samir Ziada*

Department of Mechanical Engineering, McMaster University, Hamilton, Ontario, Canada
*corresponding author: ziadas@mcmaster.ca

Abstract A simplified model of a landing gear, consisting of a strut and two circular lights, is tested in a wind tunnel to investigate the effect of the landing light position on the resulting pressure fluctuations and the flow structure in the near-wake of the landing gear. Measurements of the pressure fluctuations in the wake, combined with phase-locked Stereoscopic Particle Imaging Velocimetry (SPIV) of the unsteady wake identified two predominant sources of pressure fluctuation, each with a unique frequency and location within the near-wake. The higher frequency source of pressure fluctuations is characterized by a relatively wide frequency band centered at a Strouhal number of 0.33 and is situated in the outer regions of the wake, immediately downstream the landing lights. On the other hand, the lower frequency source produces narrow band pressure fluctuation at a Strouhal number of 0.11 and is developed further downstream and closer to the wake centerline. Phase-locked, time-resolved SPIV analysis is performed to obtain the details of the three-dimensional mean and fluctuation velocity fields. Changing the distance between the lights, within the tested range, does not affect the main characteristics of the lower frequency source. However, the higher frequency pressure source becomes weaker and almost vanishes when the distance between the lights and the landing gear strut becomes small.
Keywords: landing gear noise, stereoscopic particle image velocimetry, wake structure of a landing gear

1 Introduction

Airframe noise generation of aircrafts has received considerable attention in recent years because of the substantial progress achieved in reducing the engine noise. For example, airframe noise, including the noise generated by the landing gear, becomes the dominant noise source when the engine is running at low power during the landing approach [1], [2]. Typically, landing gears consist of several components of different shapes and sizes, such as wheels, struts, lights, hydraulic cables, and others. Therefore, landing gear noise spectra are generally spread over a wide range of frequency [3],[4]. Most of the work in the literature is focused on measuring or computing the far field noise characteristics for various landing gear configurations [3]-[7]. Various methods to alleviate the noise generation mechanisms and reduce the level of noise generation by landing gears have also been reported, see for example [8]-[10].
While the noise generated by the wheel assembly has received considerable attention in previous studies, little effort has been made to better understand the effects of proximity between the lights and the strut, as typically found in the front landing gear assembly, on the noise generation mechanism, even though the lights-strut assembly has been identified as a significant contributor to the overall noise emissions [2].
Since the unsteady flow field in the landing gear near-wake is the main source of noise generation, the present study focuses on the pressure fluctuations in this region with particular emphasis on the effect of the landing lights positions on the distribution and frequency content of the fluctuating pressure field in the wake. A simplified model of the landing gear is used which allows the landing light spacing to be varied relative to the strut. The landing lights are modelled to resemble the main geometry features observed in practice, including both the circular shape and tapered after body. The three-dimensional distribution of the pressure fluctuation is first mapped over the near-wake of the landing gear for several flow velocities. This is performed for three different positions of the landing lights relative to the strut. The unsteady time resolved flow field is then quantified using particle imaging velocimetry for two of the landing light positions which show different pressure fluctuation characteristics.

2 Test set-up

A simplified model of an aircraft front landing gear is tested in a wind tunnel. The model shown in Fig. 1 consists of a single cylindrical strut and two landing lights evenly spaced on opposing sides of the strut. It is fabricated from PVC due to its ability to reduce the reflections of the laser sheet employed by the SPIV. The diameter of the strut and the lights is D=42 mm and all other dimensions are given in Fig. 1. The lights are

secured in position by means of thin aluminum beams 1.6 mm in thickness. Beams with different lengths are used to test three values of the center-to-center distance between the lights and strut, L=0.8D, 0.9D and 1.0D. Adequate measures have been implemented to minimize the noise generated by the supports [11]. The strut has also been tested in the wind tunnel with and without the thin beams and the results have shown that no significant noise emissions are produced when the supports are added.
The model is tested in a low speed open-circuit wind tunnel. As the dimensions of the wind tunnel test section are 711x216 mm, the model creates a small blockage ratio of 6.9%. As shown in Fig. 2, a custom test section is built for which the top and bottom walls are extended by 510 mm using 11.9 mm thick acrylic plates. Due to the wide shape of the wind tunnel, the sides are not extended because they are sufficiently far from the test model. The wind tunnel air speed is calibrated with the aid of a Pitot tube.

2.1 Measurement of pressure fluctuations

The characteristics of pressure fluctuations are mapped in the near-wake of the landing gear. Referring to Fig. 1, the pressure measurements span 5.6D downstream of the landing gear in the y-direction, 2.4D in the x-direction from the center of the strut, and 1.0D above and below the center of the lights in the z-direction. The measurements are obtained by traversing a microphone with a grid spacing of 10 mm. The G.R.A.S. condenser microphone system used to perform the measurements consists of a ¼” microphone type 40CP, a preamplifier type 26AC, and a power supply type 12AA. The microphone is equipped with a blunt tipped nose cone to reduce unwanted pressure fluctuations caused by flow interaction with the microphone. A computer controlled three axis traverse is used to move the microphone in the wake. National Instruments 9233 data acquisition device with four 24 bit IEPE analog inputs is used to record the pressure signal.
The pressure fluctuation amplitude is presented as normalized pressure, P^*, as a function of Strouhal number, St. These are defined as:

$$P^* = P_{\max} / (\tfrac{1}{2} \rho V_m{}^2) \tag{1}$$

$$St = f\, D/V_m \tag{2}$$

These variables are defined using the maximum RMS fluctuation pressure, $P_{\max}$, frequency, f, density of the working fluid, ρ, mean flow velocity in the wind tunnel, V_m, and the diameter of the strut, D.

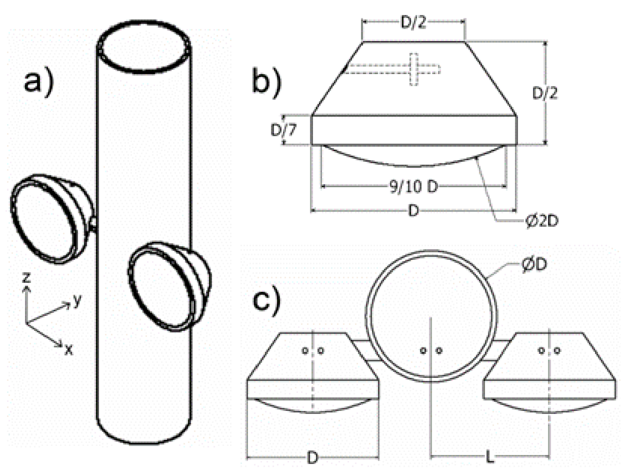

Fig. 1 Schematic of simplified landing gear model, including (a) isometric diagram of the model, (b) dimensioning of light relative to strut diameter and (c) aerial view of model with appropriate length scales studied

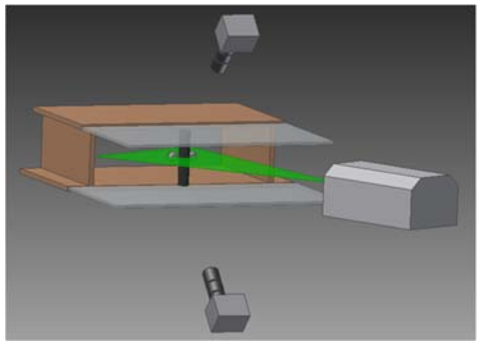

Fig. 2 Schematic of the SPIV apparatus

2.2 Particle image velocimetry

A stereoscopic particle imaging velocimetry (SPIV) system is utilized as is illustrated in Fig. 2. The system includes a 532 nm New Wave Solo 120XT pulsed Nd:YAG laser along with two 12 bit Power View 4MP CCD cameras and accompanying Nikon AF Nikkor 50 mm lenses. An optical bandpass filter centered at 532 nm and containing a bandwidth of 10 nm is situated at the end of each camera lens to filter light which does not originate from the laser. The cameras and laser are synchronized using a TSI LaserPulse Model 610035 synchronizer. One camera is located on each side of the laser sheet at an angle of 45°. To realign the plane of focus with the light sheet, the CCD sensor is angled relative to the lens such that the Scheimpflug condition is satisfied. Furthermore, a Laskin aerosol generator is used to seed the flow with bis (2-ethylhexyl) sebacate with a mean particle diameter of 1 µm.

The camera frames are calibrated using a calibration target with a well-defined fiducial marker. To remove the error associated with the placement of the target relative to the light sheet, the disparity between the frames is minimized using a 'StereoAutomapping' algorithm in Insight 3G, a self-calibration process outlined by Wieneke [13] which dewarps and cross-correlates image pairs taken simultaneously by each camera at an instance in time. Care is taken to ensure neither the light sheet nor the cameras are moved between the time the images are taken and when the calibration process is performed. Insight 3G is also used to capture and process the SPIV images. The images are processed using the Classical PIV algorithm over a 16 pixel square deformation grid with vector validating rates consistently in excess of 99%. As discussed below, there are two frequency components of the pressure fluctuations, each dominates over a different region of the wake. Image processing entailed taking 200 phase-locked image pairs by each camera at the same time instant within the flow oscillation cycle. These are then processed and averaged to obtain phase-locked averaged images of the velocity field at eight instances evenly spaced along the cycle of the lower frequency oscillation. The microphone signal, when positioned near the location of the maximum pressure fluctuation, is used to trigger the SPIV system. This signal is filtered using a band-pass filter centered at the lower frequency of pressure oscillation. However, this approach of acquiring phase-locked images could not be performed for the high frequency component because its broad-banded nature inhibited the ability to repeatedly trigger the camera at the same time instant in the oscillation cycle. To improve the resolution, the SPIV images are taken over 80% of the flow field, however the results displayed hereafter correspond to only one half of the flow field ($x \geq 0$), and are mirrored over the other half accounting for the out-of-phase relationship between the two sides of the wake. This method of data presentation has been validated by comparisons with the images taken over 80% flow field. The averaging and further processing of the images is completed in MATLAB and Tecplot.

The Reynolds stress is calculated from 200 SPIV images taken randomly over the acoustic cycle and is calculated using predefined functions in Tecplot. The Reynolds stress provides insight into the momentum flux between various components of the velocity field and ultimately the three-dimensional characteristics of the flow.

3 Pressure fluctuations in the near-wake

This section focuses on mapping the unsteady pressure field in order to better understand the origin of various noise sources in the landing gear wake. Two regions of pressure fluctuations at different frequencies were observed. The lower frequency region (hereafter referred to as the f_1 source) is associated with the shear flow originating from the gap between the strut and the lights, while the higher frequency region (hereafter referred to as the f_2 source) is generated by the separated flow around the lights. A third distinct source was also observed, however only in regions far above and below the light elevation, the frequency of which corresponds to a Strouhal number of 0.2, indicating that it is associated with vortex shedding from the cylindrical strut. This paper deals primarily with the pressure fluctuations generated by the complex unsteady flow pattern due to the addition of the lights, i.e., with the pressure sources f_1 and f_2.

The sample pressure spectra shown in Fig. 3 are taken at two different locations, where the fluctuation amplitude for each source is at its maximum in the z=0.5D plane. The spectral amplitude of pressure fluctuation for both sources varies with the spatial location within the wake, however the frequency does not. The low frequency source, f_1, persists at a Strouhal number of 0.11 and has a relatively narrow frequency band. However, the f_2 source has a Strouhal number of 0.33 and exhibits a wider frequency band. While the frequency f_2 does appear to be an integer multiple of f_1, they occur in different regions and their frequency bands have different characteristics. Thus, they do not appear to be harmonics of each other. As can be observed from Fig. 3, both sources show virtually constant Strouhal number for the tested velocity range.

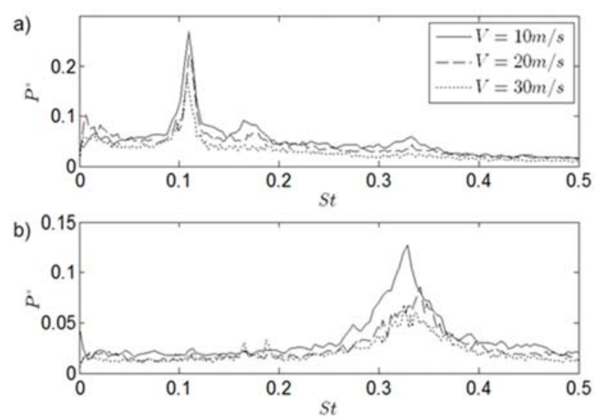

Fig. 3 Sample pressure spectra for flow velocities of 10 m/s, 20 m/s and 30 m/s for both (a) the lower frequency source f_1 and (b) the higher frequency source f_2

Figures 4 and 5 show the amplitude distributions of the fluctuating pressure at both frequencies (f_1 and f_2) for the largest light spacing (L=1.0D) and at a flow velocity of 30 m/s. The plane through the light centers is taken to be the z=0 plane. The plots in each of these figures correspond to various elevations, starting from the center plane (Fig. (a) for z=0) to below the lights (Fig. (d) for z=D). Interestingly, the magnitude of the fluctuating pressure decreases from the center plane to the bottom of the lights, then increases again a quarter diameter below the lights, and finally becomes substantially weaker further below the lights. The distribution of the pressure amplitude for f_2, shown in Fig. 5 is more localized than f_1 as the pressure fluctuations around the edges of the lights are not observed below the plane z=0.5D. There are two separate regions where this source exists, the inner and outer regions. The outer region fluctuations appear to follow the outer perimeter of the lights and disappear slightly below the lights (z=0.75D). The inner region fluctuations follow a similar trend to the f_1 pressure distribution as the magnitude decreases from the center plane to the bottom of the lights, increases slightly below the lights and then decreases again.

Amplitude distributions of pressure fluctuations similar to those shown in Figs. 4 and 5 were also obtained for additional two flow velocities, 10 m/s and 20 m/s. However, for brevity, they are not presented here because they showed similar characteristics to those discussed for the case of 30 m/s. While the Strouhal number, St, and the general shape of P^* distribution for both sources did not change with flow velocity, the pressure distribution is observed to shift slightly upstream for higher flow velocities. The overall movement of both sources from the lowest flow velocity (V_m=10 m/s) to the highest flow velocity (V_m=30 m/s) is approximately a quarter diameter. This is not overly surprising as it is expected that the wake develops faster at higher flow velocities.

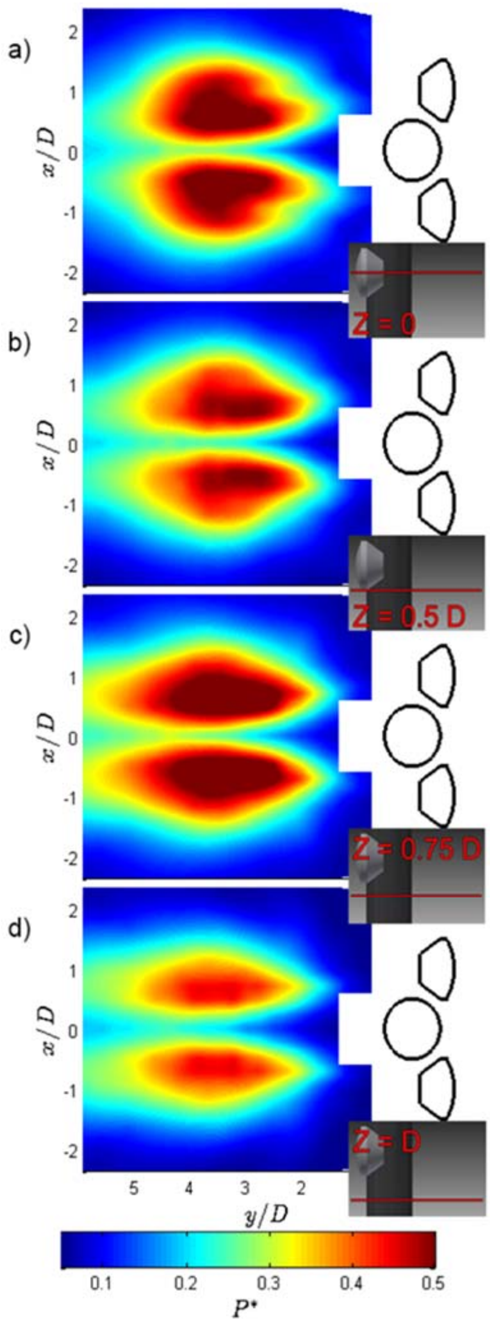

Fig. 4 Pressure amplitude distribution of the f_1 source for planes (a) z=0, (b) z=0.5D, (c) z=0.75D and (d) z=D

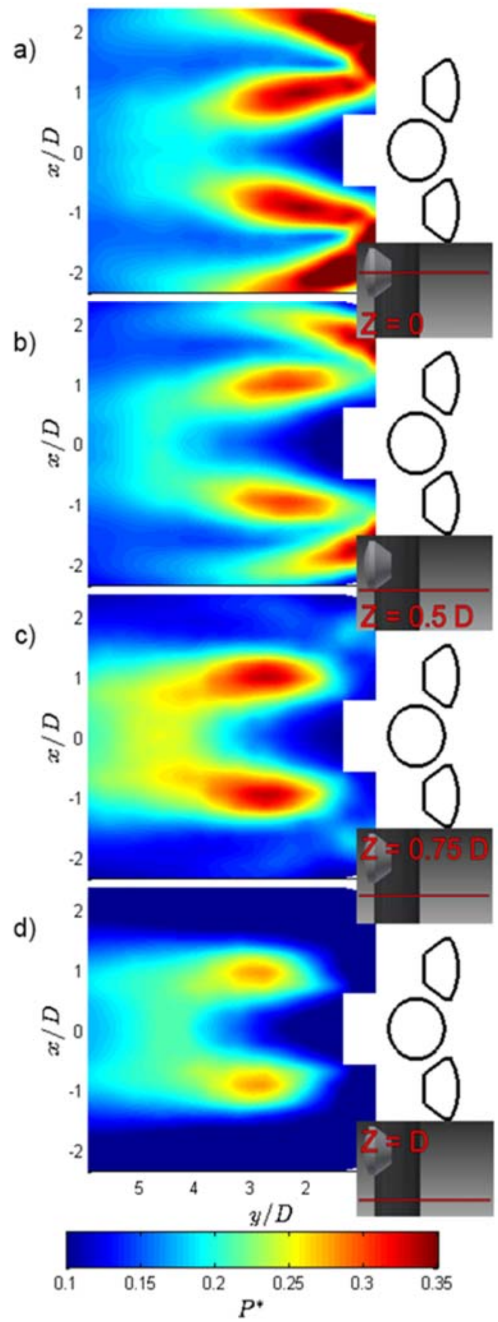

Fig. 5 Pressure amplitude distribution of the f_2 source for planes (a) z=0, (b) z=0.5D, (c) z=0.75D and (d) z=D

4 Time resolved flow field for f_1 frequency component

The time resolved velocity and vorticity fields for the f_1 oscillation cycle are given in Fig. 6 for the center plane (z=0). The figure shows the images at two time instants separated by 180° for the largest light spacing ($L = 1.0D$) which generates the strongest pressure fluctuations. The three-dimensional velocity magnitude with two-dimensional streamlines are shown on the left side and the two-dimensional vorticity field with the

corresponding d_2 parameter are displayed on the right side. The d_2 parameter is defined as the discriminant of the velocity gradient tensor as proposed by Vollmers [14] and is very useful for identifying propagating near-circular vortical structures. The vorticity field reveals alternating shedding of flow structures at the frequency f_1 in the extended wake formed behind the strut and the lights. Since the vertical velocity component (w) in this center plane is found to be small in comparison with the other velocity components, the flow field in this plane can be considered to be predominantly two-dimensional. The inherent three-dimensional effects on pressure fluctuations and noise generation will be discussed later.
As can be seen in Fig. 6, there are two regions with velocity gradients (i.e., shear flow regions) on each side of the wake centerline. One region is formed by the flow between the light and the strut, while the other is formed around the outer perimeter of the lights. The vortices responsible for the f_1 source originate from the shear flow located between each light and the strut, while the shear flow around the outer perimeter of the lights is responsible for the f_2 source. On either side of the wake centerline, one vorticity blob forms, grows in size, then stretches and dissipates over one oscillation cycle of f_1. This is associated with significant swaying of the centerline of the velocity field over the oscillation cycle. At this center plane, the velocity profile responsible for the f_1 source appears to be similar to the case of an isolated cylinder in cross-flow. However, the frequency of the oscillations is much lower, likely a result of the earlier separation of the flow due to the presence of the lights and the resulting wider wake than in the isolated cylinder case.

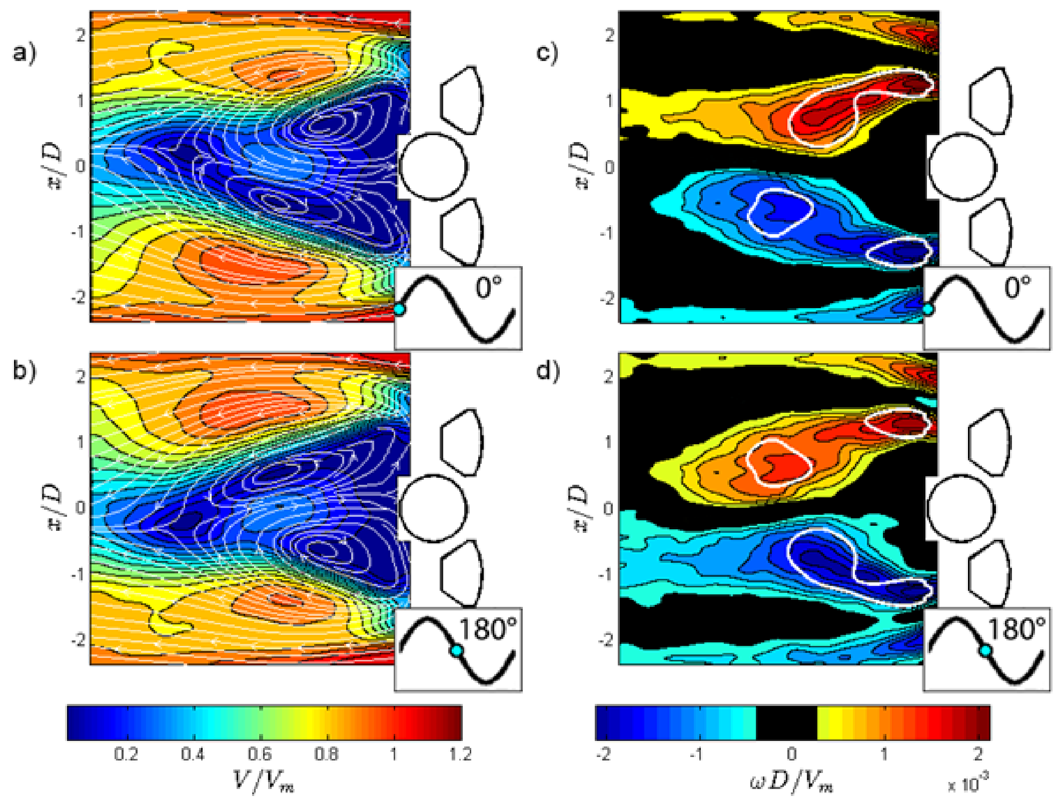

Fig. 6 Time resolved velocity and vorticity fields obtained by phase locking with the low frequency oscillation f_1. Left side: velocity magnitude $(u^2+ v^2+ w^2)^{½}$ with corresponding 2-D streamlines for two instants within f_1 oscillation cycle separated by 180°. Right side: vorticity field with corresponding d_2 parameter for two instants within f_1 oscillation cycle separated by 180°

Figure 7 compares the distributions of the fluctuation pressure amplitudes at the low and high-frequencies (insets (a) and (b), respectively) with the contours of the mean vorticity field. All three figures correspond to the center plane at z = 0. It should be recalled that the shown vorticity field represents the two-dimensional component in the x-y plane and that the other components, although not measured, are expected to be small because of the symmetry around the central plane. Since the velocity and pressure fluctuations are initiated by flow instabilities, which are triggered and amplified in vorticity fields, the fluctuating pressure field is expected to be correlated to the mean vorticity field. This correlation is exemplified in Fig. 7. The high-frequency oscillation at f_2 is produced by the vorticity field in the outer regions of the wake immediately downstream the lights (this region is denoted by f_2 in inset (c) of Fig. 7). On the other hand, the low-frequency pressure fluctuation at f_1 is produced by the vorticity field further downstream and closer to the wake centerline, which is denoted by f_1 in Fig. 7(c).

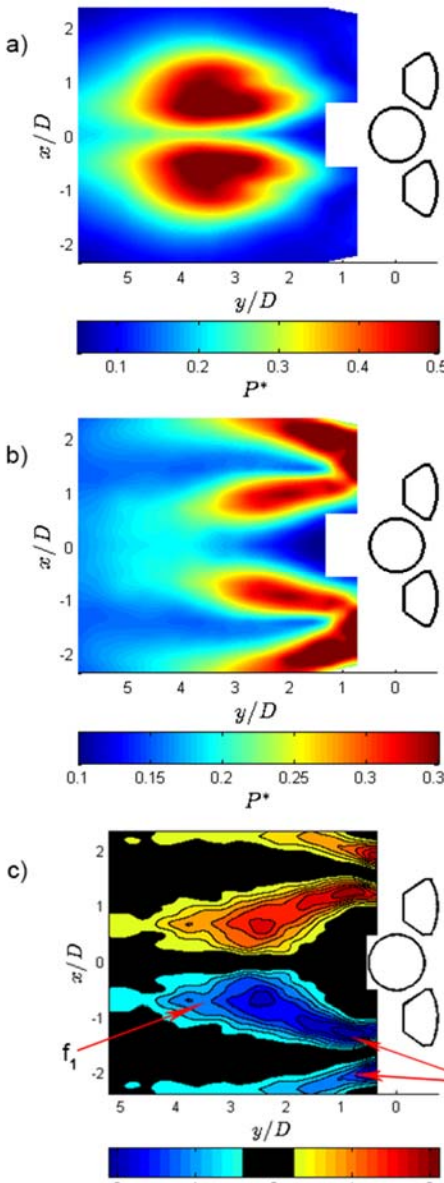

Fig. 7 Comparison of the pressure amplitude distributions for the (a) f_1 and (b) f_2 fluctuating components with (c) the mean two-dimensional vorticity field for the central plane (z=0)

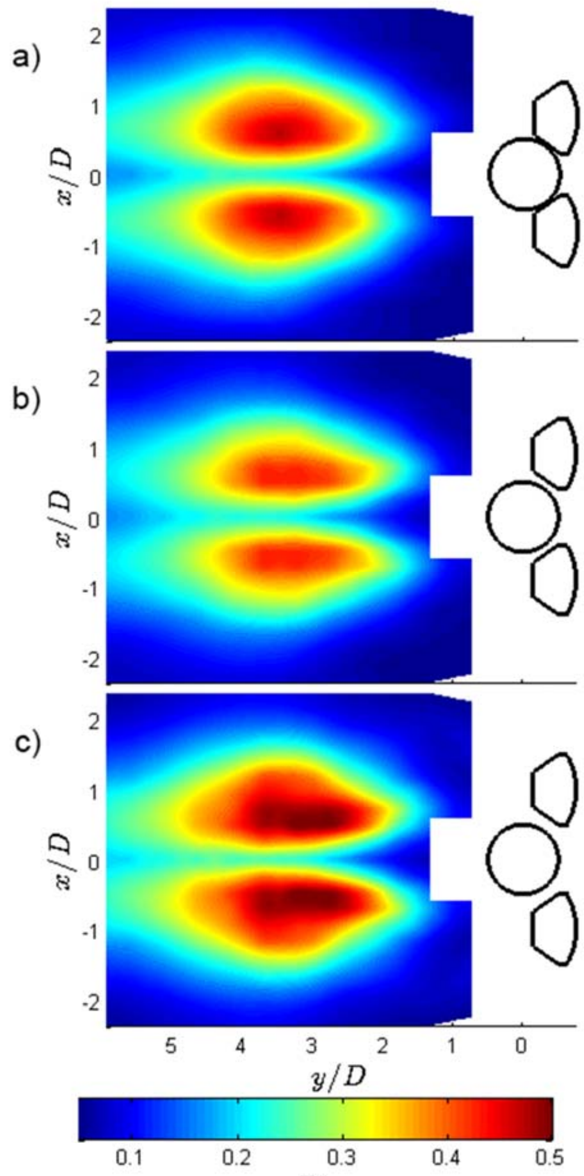

Fig. 8 Near-field pressure amplitude distribution for f1 fluctuating component in the z=0.5D plane for light spacing (a) L=0.8D, (b) L=0.9D and (c) L=1.0D

5 Effect of light spacing

The lights are tested at three lateral locations with respect to the strut. The parameter L, defined in Fig. 1(c), is used to indicate the distance between the landing lights. The value of L for the three cases is $0.8D$, $0.9D$ and $1.0D$. The lights are almost touching the strut for the smallest spacing (L=0.8D), whereas the strut becomes just outside the physical light wakes for the largest spacing (L=1.0D). Any larger spacing is considered to be outside the practical design range.

Fig. 8 depicts the distributions of pressure fluctuation for the lower frequency component f_1 for the three light spacings. The strength of the pressure fluctuations at this frequency decreases from the smallest light spacing to the intermediate spacing, and then increases significantly to the strongest case at the largest light spacing. It is important to note that no significant variation in the frequency or quality of these oscillations is observed, indicating that for the range of light spacing considered in this study, the frequency of oscillations is entirely defined by the size of the light and strut, and not the light spacing.

The higher frequency component f_2 is not plotted because it is observed for the largest light spacing only and completely disappears for both the smallest and intermediate light separations. The cause of this interesting trend is not yet fully understood, however, the following analysis of the three-dimensional velocity field does reveal important features.

The three-dimensional Reynolds stress distribution is depicted in Fig. 9 for the largest light spacing (L=1.0D) and in Fig. 10 for the smallest light spacing (L=0.8D). The mean velocity in both cases is 20 m/s. Each plot shows $u'v'$ for two elevations: (a) the center plane (z = 0), and (b) the light's lower edge plane ($z = 0.5D$). Also, $u'w'$ is shown for the same planes in insets (c) and (d) of the same figures. The third component of the Reynolds stress, $v'w'$, is smaller than the other two components by an order of magnitude and is therefore not included in this analysis. For the largest spacing case (L=1.0D), the f_1 component appears to be generated predominantly by the fluctuations in the x-y plane with the exception of a small contribution in the x-z plane from the bottom edge of the light as shown in Fig. 9(d). Interestingly, larger pressure fluctuations are observed in the center plane as shown in Fig. 4(a), however insets (a) and (b) in Fig. 9 suggest that the Reynolds stress is larger at the bottom of the lights than in the center plane. This difference may be caused by the third frequency component of pressure fluctuations. At the bottom of the lights, one may expect increased contribution to the velocity fluctuations from the aforementioned third frequency component near St = 0.2, which is attributed to the flow around the strut above and below the lights. These velocity fluctuations contribute to the Reynolds stresses shown in Fig. 9(b).

The higher frequency f_2 component, which is detected only for the largest light spacing, is observed in the region of flow separation from the outer perimeter of the lights. This region is the immediate vicinity of the lights, i.e., upstream of the region of the lower frequency oscillation. The boundary between the two domains oscillating at different frequencies (f_1 or f_2) is not clearly defined from Fig.9(d), however inspection of Figs. 4 and 5 indicates that the separated shear layer at the bottom of the lights and all the way around the outer edge of the lights do oscillate at the higher frequency f_2. Unlike the f_1 component, the f_2 fluctuation is not mainly generated by the turbulent fluctuations in the x-y plane ($u'v'$). This is because the separated flow from the lights forms a circular shaped shear layer around the perimeter of the lights, as shown in Fig. 9(d).

The Reynolds stress distributions depicted in Fig. 10 for the smallest spacing case (L=0.8D) show similar trends to those observed for the previous case with the largest spacing (L=1.0D), except that the fluctuations along the outer edge of the lights in Fig. 10(a) show much smaller magnitudes of turbulent stresses. This agrees well with the earlier near-field pressure measurements, as f_2 oscillations are not detected in the case of the smallest landing light spacing. It should be noted that a weak disturbance does appear to propagate from the outer edges of the lights for the smallest spacing case. This appears to dissipate rapidly before reaching the closest position that can be reached by the microphone. As noted earlier, the addition of the nose cone to the microphone limited the minimum distance that can be reached behind the model.

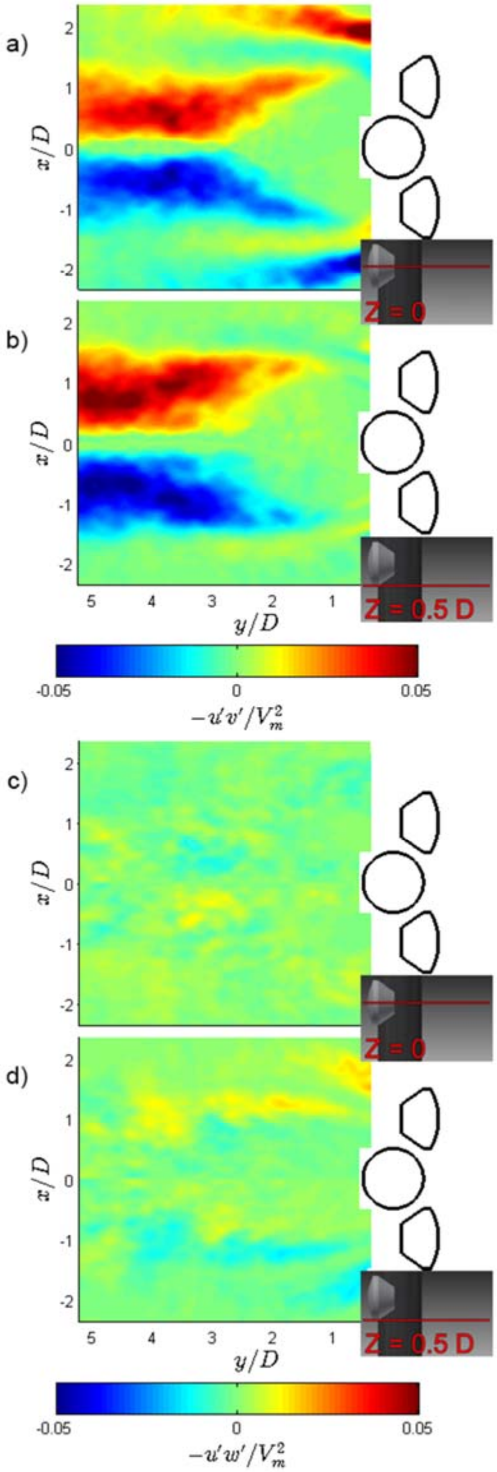

Fig. 9 Reynolds stress for the **largest** light spacing (L=1.0D) including u′v′ for both (a) the z=0 plane and (b) the z=0.5D plane, as well as u′w′ for (c) the z=0 plane and (d) the z=0.5D plane

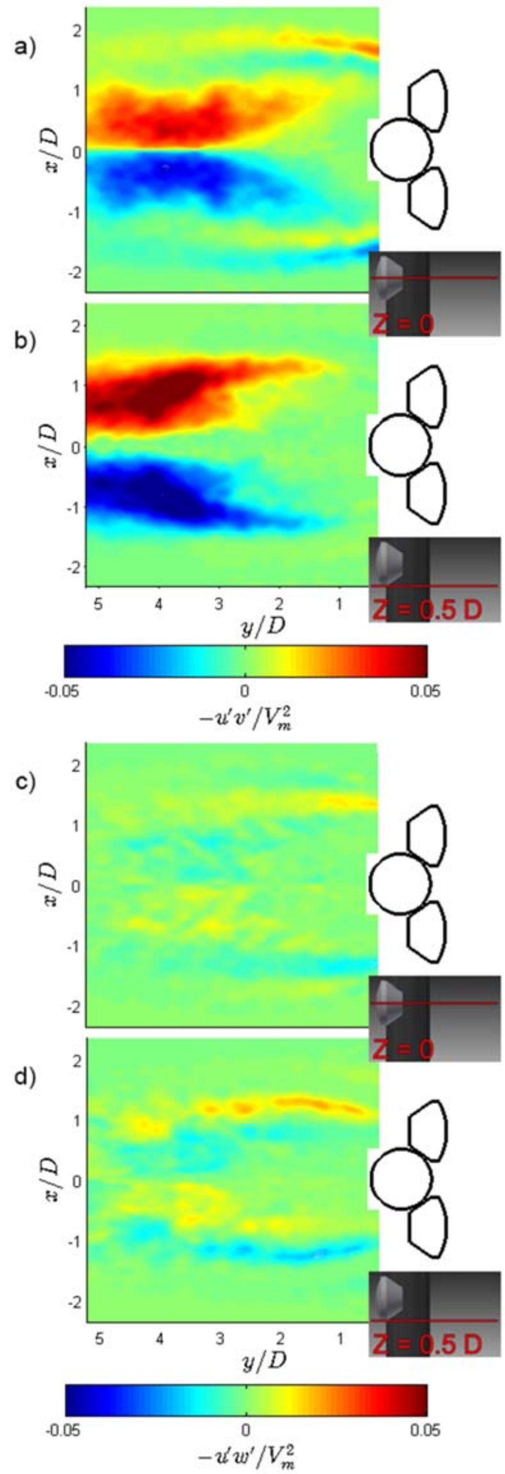

Fig. 10 Reynolds stress for the **smallest** light spacing (L=0.8D) including u′v′ for both (a) the z=0 plane and (b) the z=0.5D plane, as well as u′w′ for (c) the z=0 plane and (d) the z=0.5D plane

6 Conclusion

In this paper, the wake of a simplified landing gear model is investigated experimentally, with particular emphasis on the effect of the landing light positions, relative to the strut, on the pressure oscillation and unsteady flow structure in the wake. Two predominant frequency components of pressure fluctuation are identified in the wake of the landing gear. The pressure fluctuation at the higher frequency has a wide frequency band centered at a Strouhal number of 0.33 and is situated in the outer regions of the wake, immediately downstream of the lights. On the other hand, the lower frequency fluctuation has a much narrower frequency band at a Strouhal number of 0.11 and is developed further downstream in the wake, closer to the wake centerline. Stereoscopic PIV analysis using phase-locking techniques indicates that the low frequency component of pressure fluctuation is caused by velocity fluctuations primarily in the x-y plane, while the higher frequency pressure oscillation is more affected by velocity fluctuations in all three directions. Reducing the gap between the lights and the strut appears to suppress the high frequency pressure oscillation but has little effect on the low frequency component which continues to dominate the unsteady activities in the landing gear wake.

References

[1] Obermeier F (1980) The influence of solid bodies on low Mach number vortex sound. *Journal of Sound and Vibration*, vol. 72(1), pp. 39–49.

[2] Guo Y (2005) A statistical model for landing gear noise prediction. *Journal of Sound and Vibration*, vol. 282(1), pp. 61–87.

[3] Dobrzynski W, Buchholz H (1997) Full-scale noise testing on airbus landing gears in the German Dutch Wind Tunnel. AIAA paper No. 97-1597-CP, pp. 98.

[4] Guo Y, Yamamoto K J, Stoker R W (2006) Experimental study on aircraft landing gear noise. *Journal of Aircraft*, vol. 43(2), pp. 306–317.

[5] Lockard D P, Khorrami M R, Li F (2004) High resolution calculation of a simplified landing gear. In: proceeding of the 10th AIAA/CEAS Aeroacoustics Conference, paper No: 2004-2887.

[6] Spalart P R, Shur M L, Strelets M K, Travin A K (2011) Initial noise predictions for rudimentary landing gear. *Journal of Sound and Vibration*, vol. 330(17), pp. 4180–4195.

[7] Ffowcs Williams J E, Hawkings D L (1969) Sound generation by turbulence and surfaces in arbitrary motion. Philosophical Transactions of the Royal Society of London. Series A, Mathematical and Physical Sciences, vol. 264(1151), pp. 321–342.

[8] Dobrzynski W, Chow L C, Guion P, Shiells D (2002) Research into landing gear airframe noise reduction. In: proceeding of the 8th AIAA/CEAS Aeroacoustics Conference, paper No 2002-2409.

[9] Li Y, Smith M, Zhang X (2012) Measurement and control of aircraft landing gear broadband noise. *Aerospace Science and Technology*, vol. 23(1), pp. 213–223.

[10] Murayama M, Yokokawa Y, Yamamoto K, Hirai T (2013) Computational study of low-noise fairings around tire-axle region of a two-wheel main landing gear. *Computers & Fluids*, vol. 85, pp. 114–124.

[11] Parker R, Welsh M (1983) Effects of sound on flow separation from blunt flat plates. *International Journal of Heat and Fluid Flow*, vol. 4(2), pp. 113–127.

[12] Sumer B M (2006) Hydrodynamics around cylindrical structures. World Scientific, Singapore.

[13] Wieneke B (2005) Stereo-piv using self-calibration on particle images. *Experiments in Fluids*, vol. 39(2), pp. 267–280.

[14] Vollmers H (2001) Detection of vortices and quantitative evaluation of their main parameters from experimental velocity data. *Measurement Science and Technology*, vol. 12(8), p. 1199.

[15] Howe M (1975) Contributions to the theory of aerodynamic sound, with application to excess jet noise and the theory of the flute. *Journal of Fluid Mechanics*, vol. 71(04), pp. 625–673.